Bulletin of Engineering Geology and the Environment (2021) 80:1671–1682
https://doi.org/10.1007/s10064-020-01997-3

ORIGINAL PAPER

The characteristics of crack existence and development during rock shear fracturing evolution

Xiangxin Liu[1,2] · Lixin Wu[3] · Yanbo Zhang[2] · Shuzhi Wang[2] · Xulong Yao[2] · Xianzhen Wu[4]

Received: 6 June 2019 / Accepted: 30 September 2020 / Published online: 1 November 2020

Abstract

Rock shear fracturing occurs frequently in engineering *sites*, such as underground tunnels and rock slopes. One main factor is that the multiple presence of crack is complicated, especially in terms of crack status. This study aims to investigate the crack status from both crack existence and development. Rock fracturing is carried out by shear loading. Acoustic emission (AE) monitoring system and CCD camera are used to catch the characteristics of crack evolution. Results demonstrate that crack status is influenced by rock physical properties and its stress boundary, there exists a positive correlation between normal force and crack geometry (such as the angle of *en echelon* crack). Crack existence follows a distribution of "the whole size of *en echelon* crack and the local region of *pinnate* crack" in terms of spatial-temporal aspects. Crack development manifests the characteristics of "Inheritance and Variability".

Keywords Shear fracturing · Crack status · Crack existence · Crack development

Abbreviation

AE Acoustic emission
AF Average frequency, which is defined as AE counts divided by duration time
RA RA value, which is defined as rise time divided by maximum amplitude

Introduction

Rock shear fracturing is greatly influenced by rock mechanical properties and its stress boundary (Janach and Lan 1980; Brantut et al. 2013; Rathnaweera et al. 2017). The process of brittle rock failure is an important aspect for the safety of underground engineering (Zhou 2005; Clayton 2010). The study of activation mechanism of small- and medium-scale brittle fault is significant not only for the prediction of disasters caused by mining but also for the process of earthquake preparation (Cheng et al. 2019).

Many scholars focused on the characteristics of rock fracturing and the investigation of crack distributions. Peak shear strength and residual shear strength of rock joints within low number of cycles varied from those within high number of cycles (Hawkes and Mellor 1970; Zhou et al. 2015; Fathi et al. 2016; Liu et al. 2018). Different aperture shapes, sizes, normal stress, and shearing rates were considered to research the behaviors of unreinforced and geogrid-reinforced ballast at different rates of shearing. Interface shear strength improved significantly when the ballast was reinforced with geogrids (Sun et al. 2014; Sweta and Hussaini 2018). Present-day deformations occurring reflected complex landslides of kilometric dimensions. Interaction between predisposition factors (inherited structures, topography, slope, gravity) and triggering factors (artificial vibrations and seismotectonic activity) provided favorable conditions to slide (Dhahri et al. 2015). BPI (Block Punch Index) test was used in previous works on size effect. Failure surface initiated at the top of the specimen and propagated along it, which demonstrated that the failure did not produce by true shearing (Sulukcu and Ulusay 2001). Shear behavior of natural coal–rock interface

✉ Xiangxin Liu
liuxiangxin9@163.com

✉ Lixin Wu
awulixin@263.net

[1] College of Resources and Civil Engineering, Northeastern University, Shenyang 110819, China

[2] College of Mining Engineering, North China University of Science and Technology, Tangshan 063210, China

[3] School of Geosciences and Info-physics, Central South University, Changsha 410083, China

[4] School of Resource and Environmental Engineering, Jiangxi University of Science and Technology, Ganzhou 341000, China

was studied by performing direct shear tests under constant normal loading condition, which showed that the shearing behavior was influenced more by the strength differences between two halves rather than the surface roughness of the interface (Oyanguren et al. 2008; Li et al. 2015; Meng et al. 2016). Different varieties of Hooke's law were applied to manifest rock regional fractured under different mechanical conditions. Theoretical predictions of this method were generally consistent with empirical expressions (Liu et al. 2009). The correlation of microcracks and macroscopic shear strength was attempted to establish according to Ashby, Mohr–Coulomb failure criterion, and crack–strain relation (Moore and Lockner 1995; Li et al. 2016; Morley et al. 2018). The physics-based theory was used to explain the behavior of "Friction is high according to the rate and state Constitutive law during slow sliding, yet markedly weakens at the sliding velocity approach seismic slip speeds" (Liu et al. 2017; Aharonov and Scholz 2018). A suitable model of stress generated by freezing in open crack discussed the evolution of rock mass stability. This maximum stress generated by freezing along crack was completely defined by the pore network of the limestone matrix and crack geometry (Bost and Pouya 2017). Labaune et al. (2017) used the onset of dilatancy as the design threshold, which was a new approach to salt cavern design.

Previous studies demonstrated the characteristics of rock fracturing in many aspects. They were closely correlated with morphology characteristics, and the stress state of rock considerably affected crack propagation. However, few detailed studies analyzed the effect of cracks in spatial-temporal aspect and discussed the influencing factors of crack status. Many different scales of crack exist along rock/rock mass, and crack existence and development are important to the determined factors of crack status. In this paper, a study was focused on the crack status from the aspects of crack existence and development in terms of spatial-temporal aspects.

Rock fracturing experiment

Specimen preparation and boundary conditions

Granite specimens (150 mm × 150 mm × 150 mm, Fig. 1a) were collected from Laizhou in Shandong Province, China. Laizhou is an important gold production base in China and is rich in gold worldwide. Specimens were prepared in accordance with the Standard for Test Method of Engineering Rock Mass GB/T50266-99. Specimens were labeled from "GS-R1" to "GS-R4," where "GS" represented Granite Specimen.

Boundary conditions of rock specimens in this experiment are shown in Fig. 1b. Shear fracturing occurs in the shear plane. The rock ends do not deform in the fixed boundary. The shear loading boundary is the end of the shearing force. The normal force boundary is the end of positive stress. Furthermore, azimuth on the rock surface (Fig. 1b) is used to describe crack distributions. The upper of the rock surface is expressed as *N*, the bottom is *S*, the left is *W*, and the right is *E*.

Experimental instrument and its settings

The experimental system (Fig. 2a) is comprised of a loading system (RLW-3000, Fig. 2b), CCD camera (Pike F-421, Fig. 2c), and AE system (PCI-2, Fig. 2d). Equipment setup is guaranteed the coherence of experimental data (Ishida et al. 2017). The system is set as follows: (1) *Loading system*: the loading settings are from normal direction and shear direction. The normal force boundary is set to 300 kN (GS-R1 specimen), 250 kN (GS-R2 specimen), 200 kN (GS-R3 specimen), and 150 kN (GS-R4 specimen) at the same loading rate of 200 N/s. At the end of shear fracturing, the loading rate in the shear force boundary remains 0.2 mm/min. (2) *AE system*: sampling time is set to 0.2 μs, storage length is 2k (2048 words), recording time period is 0.4 ms, pre-trigger is 1k, and sampling rate is 1 MHz. (3) *CCD camera*: sampling speed is 16 fps, and resolution is 2048 pixels × 2048 pixels.

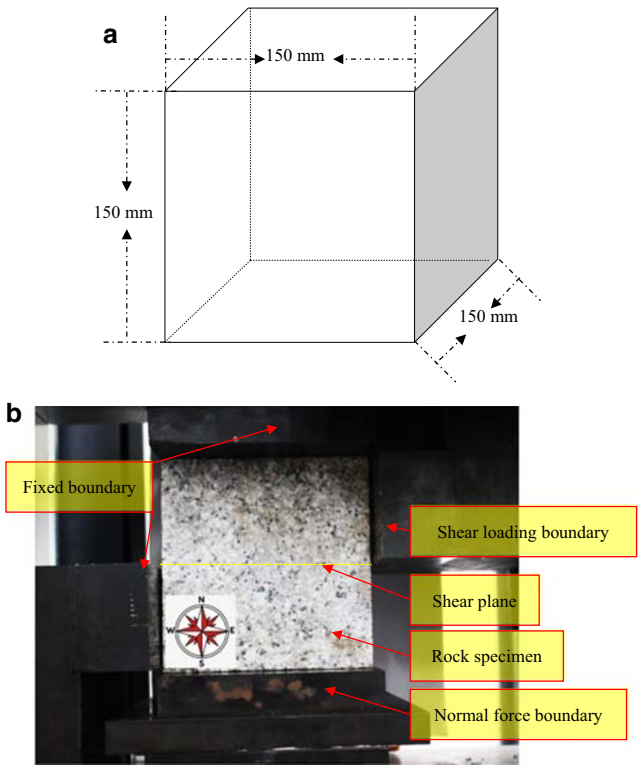

Fig. 1 **a** Rock specimen; **b** its boundary conditions

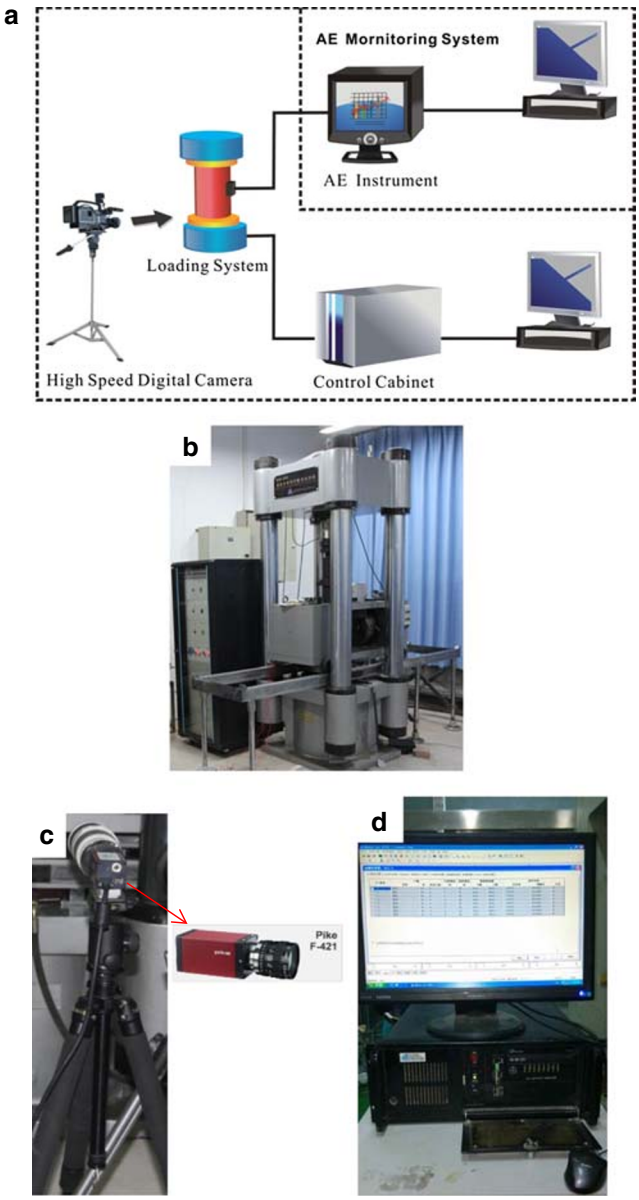

Fig. 2 Schematic diagram of the experimental setup. **a** Experiment system, **b** loading system, **c** CCD, **d** AE monitoring system

Experimental results

Stage characteristics in the shearing failure process

Shearing force, AE energy, and AE accumulative energy versus loading time are shown in Fig. 3; the final fracturing is in Fig. 4. The entire loading process is divided into three stages.

- *Phase I, initial stage*: AE activity is due to the opening or closing of micro-cracks. AE energy is low; AE accumulative energy curve increases gradually with shearing force. All specimen curves are downward.

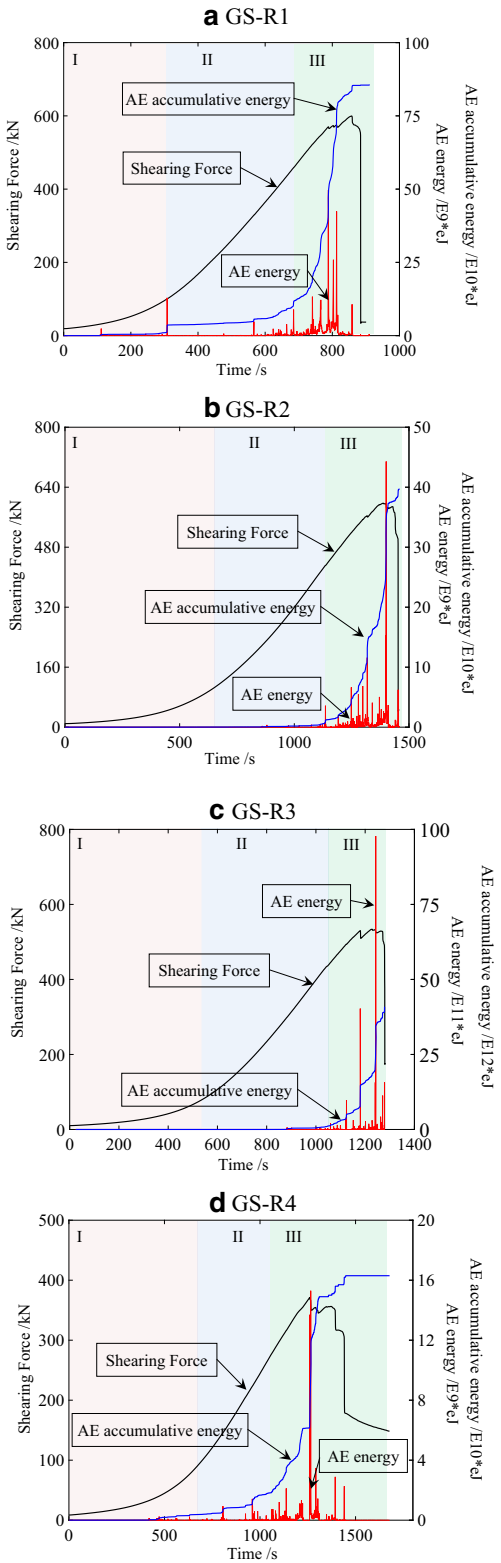

Fig. 3 Curves of shearing force and AE parameters versus time. **a** GS-R1, **b** GS-R2, **c** GS-R3, **d** GS-R4

- *Phase II, stage of crack stable expansion*: AE activity in this stage is more active than that in phase I. Shearing force curves also increase linearly.

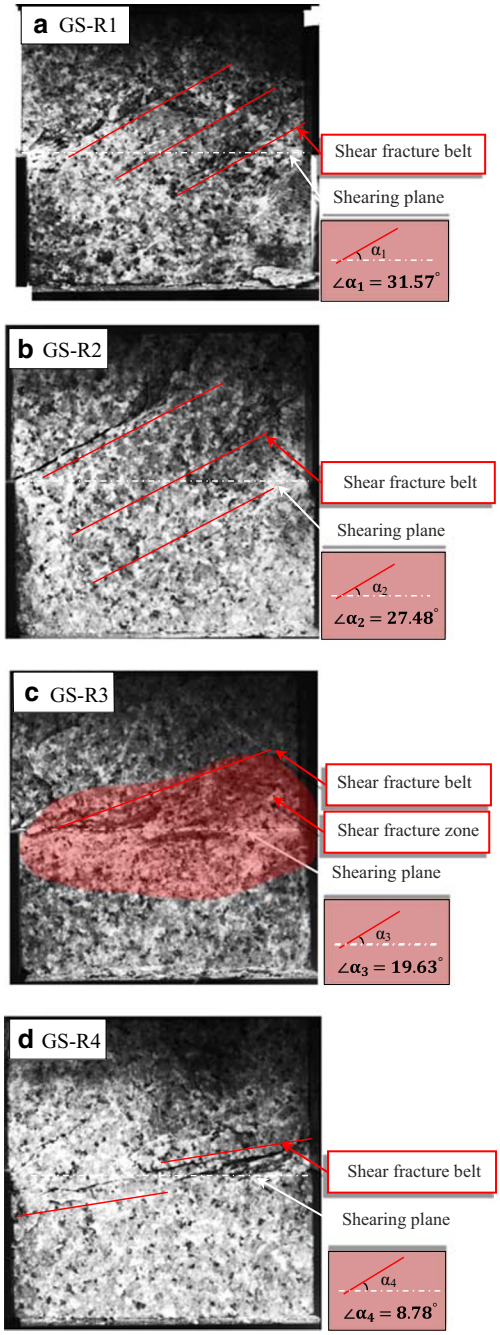

Fig. 4 Final fracturing form on four normal force levels. **a** GS-R1, **b** GS-R2, **c** GS-R3, **d** GS-R4

- *Phase III, stage of crack unstable expansion*: AE activity is more active than that in phases I and II. AE activity is extremely active, and the curves of AE energy and AE accumulative energy rise up vertically. Weakened rock specimens do not bear such great amount of shearing strain energy, then final failure occurs.

The final fracturing form

According to the different normal force, the characteristics of *en echelon* are not the same, which are similar to dip (α) of *en echelon* (Fig. 4). $\angle\alpha_{GS-R1}$ of *en echelon* of GS-R1 specimen ($F_N = 300$ kN) is 31.57° (Fig. 4a), $\angle\alpha_{GS-R2}$ of *en echelon* of GS-R2 specimen ($F_N = 250$ kN) is 27.48° (Fig. 4b), $\angle\alpha_{GS-R3}$ of *en echelon* of GS-R3 specimen ($F_N = 200$ kN) is 19.63° (Fig. 4c), and $\angle\alpha_{GS-R4}$ of *en echelon* of GS-R1 specimen ($F_N = 150$ kN) is 8.78° (Fig. 4d). A crack splits into a series of *en echelon* crack, such as shear fracture belt in Fig. 4a~d. The crack surface does not twist and remains a single continuous surface, which may appear a series of small cracks in *en echelon* arrangement.

A positive correlation exists between normal force and angle (α) of *en echelon*. The entire angle is less than 45°, and *en echelon* produces under shearing condition (Pluijm and Marshak 2004). With increasing shearing force, the angle of shearing force and normal force changes, but α does not change. It turns out to be that the only constant factor is the normal force. Then, the shear force guarantees rock unstable failure, and normal force keeps crack directivity.

Crack spacing characteristics

According to the curve of shear force versus time (Fig. 3) and the final fracturing form (Fig. 4), crack existence and development have the following characteristics (Fig. 5).

Phase I (**a** and **b** in Fig. 5), the initial stage is divided into two parts. One part is the unruptured time (**a** in Fig. 5). Internal crystal crack occurs in shear plane and vicinity of granite specimen, it forms "X"-style shape ($\mathbf{C1_1}$ and $\mathbf{C1_2}$ in Fig. 5.1a, $\mathbf{C2_1}$ and $\mathbf{C2_2}$ in Fig. 5.2a, $\mathbf{C3_1}$ and $\mathbf{C3_2}$ in Fig. 5.3a, $\mathbf{C4_1}$ and $\mathbf{C4_2}$ in Fig. 5.4a). The other part is the initial fracturing time (**b** in Fig. 5). In the center of shear plane, cracks begin to develop from two sides of granite specimen to the center, which are similar to crack groups of $\mathbf{C1_3}$ – $\mathbf{C1_5}$ in Fig. 5.1b, $\mathbf{C2_3}$ – $\mathbf{C2_4}$ in Fig. 5.2b, $\mathbf{C3_3}$ – $\mathbf{C3_4}$ in Fig. 5.3b, and $\mathbf{C4_3}$ – $\mathbf{C4_4}$ in Fig. 5.4b.

Phase II (**c** in Fig. 5), crack continues to grow in horizontal and vertical directions. The main crack type is *pinnate* crack in mesoscale, such as $\mathbf{C1_8}$, $\mathbf{C1_9}$, and $\mathbf{C1_{10}}$ in Fig. 5.1c, $\mathbf{C2_5}$ and $\mathbf{C2_6}$ in Fig. 5.2c, $\mathbf{C3_5}$ and $\mathbf{C3_7}$ in Fig. 5.3c, $\mathbf{C4_3}$ in Fig. 5.4b and $\mathbf{C4_6}$ and $\mathbf{C4_8}$ in Fig. 5.4c. Crack on center initially forms a dense cleavage belt, and interspace of cleavage planes are approximately 2 mm. Small-angle intersections stagger between some secondary fracture planes and general direction of shearing zone.

Almost all cleavages propagate by *en echelon* model. *en echelon* shows different scales, which vary from 1 to 35 mm, indicating a feature of self-similarity structure. GS-R1 specimen is the most active in developed fracturing, and $\mathbf{C1_6}$ – $\mathbf{C1_{10}}$ crack group exists. GS-R2 specimen

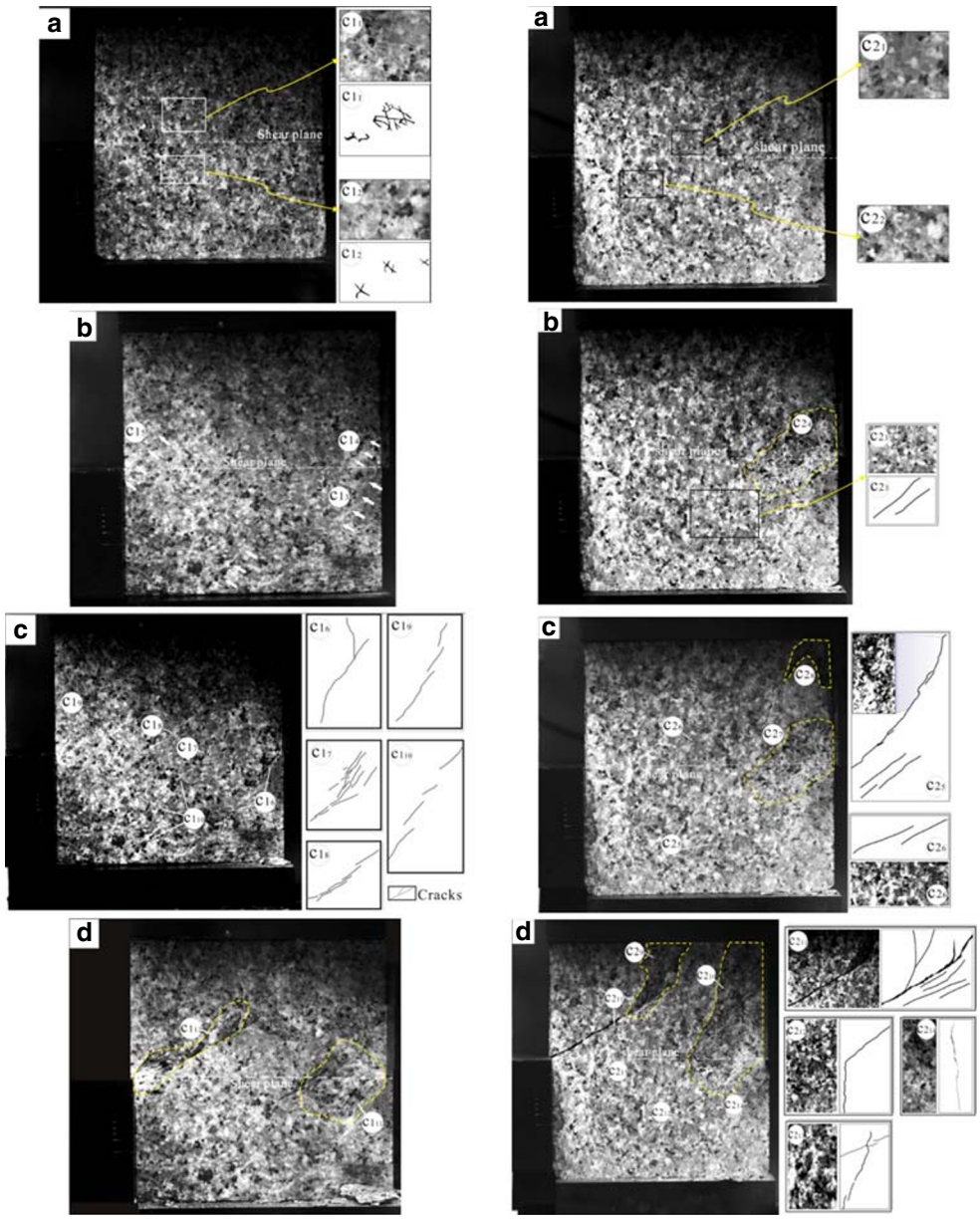

(1) GS-R1 (Normal force = 300 kN) (2) GS-R2 (Normal force = 250 kN)

Fig. 5 Rock fracturing evolution in different normal force levels

has two peeled surfaces, named $\mathbf{C2_7}$ and $\mathbf{C2_8}$. The characteristic of crack directions in GS-R3 specimen is located on both sides of the shear plane. Crack distribution area in GS-R4 specimen is larger than that in GS-R3 specimen.

Phase III (**d** in Fig. 5), *en echelon* crack represents a basic characteristic of fault combination (Fig. 5.1d, Fig. 5.2d, Fig. 5.3d, and Fig. 5.4d). In response to the rock spalling, GS-R1 specimen appears in $\mathbf{C1_{11}}$, GS-R2 specimen in $\mathbf{C2_{10}}$ and $\mathbf{C2_{14}}$, and GS-R3 specimen as a big rock spalling along the shear plane and forms a spalling zone of $\mathbf{C3_9}$. GS-R4 specimen does not show obvious rock spalling but forms a crack concentration zone of $\mathbf{C4_{12}}$. Lateral growth of cracks, which can be accomplished by the migration of incoherent boundary, occurs simultaneously in response to cracking. All the dense cracks, including *en echelon* cleavages and gently inclined cleavages, interpenetrate, leading to the surface peeling off in this stage. In horizontal direction, the strength of rock failure follows the trend of "strong → weak → strong."

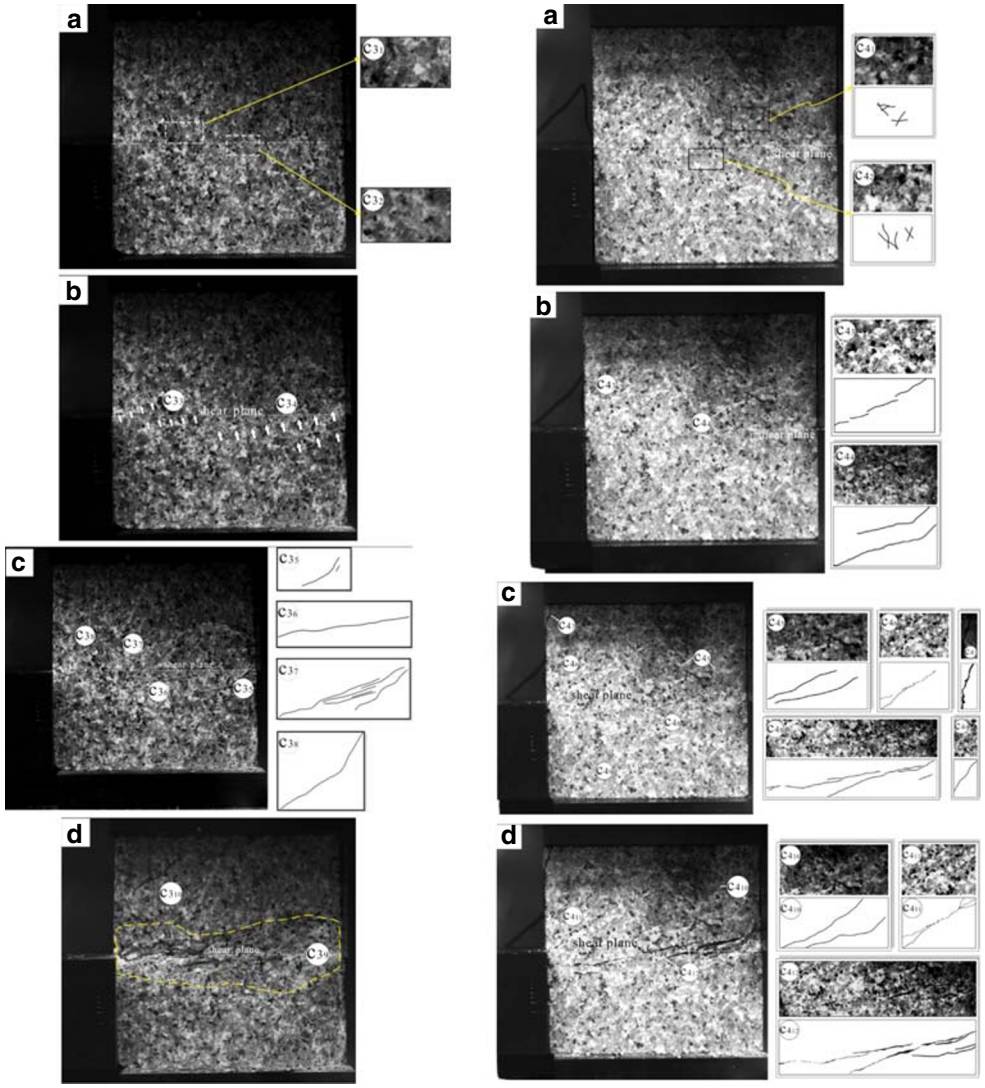

(3) GS-R3 (Normal force = 200 kN) (4) GS-R4 (Normal force = 150 kN)

Fig. 5 continued.

Crack mode characteristics

In this part, the degree of fracturing and the fracturing capacity of different specimens were discussed in terms of cumulative energy, ringing count, duration time, and energy index (Xu et al. 2017). It formed the distribution of disturbance stress, which was in an unstable state. RA-AF's relationship reflected crack model; equations for both types were presented in Eqs. (1) and (2) (Ohtsu et al. 2007a; Shiotani 2008).

$$\mathrm{RA} = \frac{\text{Rise Time}}{\text{Amplitude}} \tag{1}$$

$$\mathrm{AF} = \frac{\text{Counts}}{\text{Duration Time}} \tag{2}$$

Crack type is classified according to the following factors (Fig. 6), (1) mode I, tensile crack has high AF values and low RA values; and (2) mode II, shear movement had low AF values and high RA values (Farhidzadeh et al. 2014).

According to Eqs. (1) and (2), the predefined diagonal lines in figures were based on flexural, tensile, and direct shear tests in laboratory systems (Ohtsu et al. 2007a). As normal force decreases, the crack type in the early state is inversely proportional to shearing crack (Fig. 7).

- In GS-R1 specimen (Fig. 7(1)), tensile and shearing cracks develop. In the loading process, shearing crack develops faster. The developed tensile crack becomes less during unstable expansion (phase III).
- In GS-R2 specimen (Fig. 7(2)), the phenomenon of pure tensile crack exists in phase I. After tensile crack generation, cracks open immediately, and the surface of open crack never touches mutually, and slip does not occur. Initially, AE

signals that produced by tensile crack dominate the detected emissions, whereas the representing shear fracturing increases.

- In GS-R3 specimen (Fig. 7(3)), unlike other conditions, shearing crack is the main crack type in phase I. The number of tensile cracks is positively correlated to shear force.
- In GS-R4 specimen (Fig. 7(4)), AE mainly generates from new tensile microcracks when the stress level is low, which is similar to that in GS-R2 of phase I. In the entire process, little shearing cracks form, but the proportions of shear fracture increases.

Results

Cracking development in the entire shearing process

Failure modes under shearing test are influenced by the normal force. As for crack distribution and fracturing degree under the effect of normal force, crack existence is discussed in terms of inheritance and variability based on the scale of space-time (Fig. 8). In this experiment, stress boundary of rock specimen forms in two aspects, namely, normal force and shear force. Cracks display parallel *en echelon* and end-to-end alignment, that is a vein zone (Crack patterns in Fig. 8). Crack group in macrocosm scale forms a type of *en echelon*, which is similar to those in $\mathbf{A1_1}$ and $\mathbf{A1_2}$ and $\mathbf{A1_4}$ (GS-R1 in Fig. 8.(1)), $\mathbf{A2_1}$, $\mathbf{A2_2}$, **and** $\mathbf{A2_3}$ (GS-R2 in Fig. 8.(2)), $\mathbf{A3_1}$, $\mathbf{A3_2}$, and $\mathbf{A3_3}$ (GS-R3 in Fig. 8.(3)), $\mathbf{A4_1}$, $\mathbf{A4_2}$, $\mathbf{A4_3}$, and $\mathbf{A4_4}$ (GS-R4 in Fig. 8.(4)). In addition, crack tip of shear pivoted to a new orientation from free surface (no cohesion) (Misra et al. 2009). Crack splits into a series of small *pinnate* cracks model because crack surface still single and continuous, and it may appear as a series of small cracks in a *pinnate* arrangement. Crack extending in localization scale forms a *pinnate* crack, which is similar to those in $\mathbf{A1_1}$ and $\mathbf{A1_3}$ (GS-R1 in Fig. 8.(1)), $\mathbf{A2_1}$ and $\mathbf{A2_2}$ (GS-R2 in Fig. 8.(2)), $\mathbf{A3_1}$ and $\mathbf{A3_2}$ (GS-R3 in Fig. 8.(3)), $\mathbf{A4_1}$, $\mathbf{A4_2}$, $\mathbf{A4_3}$, and $\mathbf{A4_5}$ (GS-R4 in Fig. 8.(4)).

Crack geometry is quantified by crack patterns, Fisher concentrations, and crack percentage (Fig. 8). Fisher method is used as a projection method. Compared with crack distributions in phase I, crack distribute randomly, the angle is from 0° to 90° uniformly (*a* in Fig. 8). In phase II, crack distribution manifests a relevance to normal force, maximum percentage of crack angle on GS-R1 specimen ($F_N = 300$ kN) is in the range of 60°~70°, GS-R2 specimen ($F_N = 250$ kN) is 30°~40°, GS-R3 specimen ($F_N = 200$ kN) is 20°~30°, and GS-R4 specimen ($F_N = 150$ kN) is 10°~20° (crack percentage of *b* in Fig. 8). In phase III, cracking develops rapidly (*c* in Fig. 8). Compared with the crack distribution in phase II, phase III keeps the same status, and crack development remains in the same orientations (Fisher concentrations of *c* in Fig. 8). The maximum percentage of crack angle of different rock specimens is also the same (crack percentage of *c* in Fig. 8).

Scale effect of crack

Rock fracturing process is multi-scale. In the end, a macroscopic-scale catastrophism phenomenon occurs. In the "The final fracturing form" section, the microscale of fracturing begins in the form of transgranular cracks, mesoscale develops from the localized grains clusters in the form of *pinnate* crack, and macroscale derives from the whole size of rock specimen in the form of *en echelon* crack.

Whereas crack development is cross-scale, and cross-scale distributes along micro-, meso-, and macroscales (Li and Tang 2015). (1) In microscale, cracks are mainly "X"-shaped conjugates, such as $\boldsymbol{C1_1}$ and $\boldsymbol{C1_2}$ in Fig. 4.1a, $\boldsymbol{C2_1}$ and $\boldsymbol{C2_2}$ in Fig. 4.2a, $\boldsymbol{C3_1}$ and $\boldsymbol{C3_2}$ in Fig. 4.3a, $\boldsymbol{C4_1}$ and $\boldsymbol{C4_2}$ in Fig. 4.4a. Cracks in microscale are in good agreement with all the rock specimens. "X"-shaped crack is mainly shearing crack. From RA via AF (Fig. 7.a), the most common crack belongs to tensile type. (2) In mesoscale, cracks are mainly *pinnate* model. *Pinnate* is the secondary crack, such as $\boldsymbol{C1_7}$, $\boldsymbol{C1_8}$, $\boldsymbol{C1_9}$, and $\boldsymbol{C1_{10}}$ (Fig. 4.1c), $\boldsymbol{C2_5}$ and $\boldsymbol{C2_6}$ (Fig. 4.2c), $\boldsymbol{C2_{11}}$, $\boldsymbol{C2_{13}}$ and $\boldsymbol{C2_{14}}$ (Fig. 4.2d), $\boldsymbol{C3_7}$ (Fig. 4.3c), $\boldsymbol{C4_3}$ (Fig. 4.4b), $\boldsymbol{C4_6}$ and $\boldsymbol{C4_8}$ (Fig. 4.4c), $\boldsymbol{C4_{11}}$ and $\boldsymbol{C4_{12}}$ (Fig. 4.4d). The acute angle between *pinnate* cracks and fracturing indicated the sense of shear in shearing plane (Engelder 1989; Alsop and Holdsworth 2004; Wei et al. 2011; Winter et al. 2017). From Fig. 7.b, the proportion of shearing crack mode increases. Hence, the main crack type in mesoscale is shearing crack. (3) In

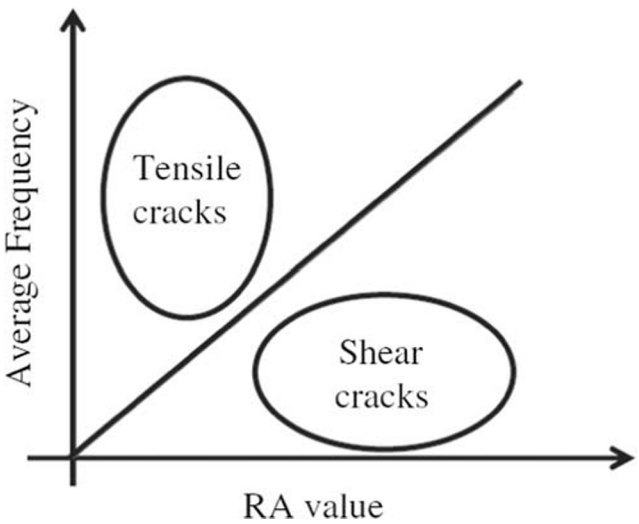

Fig. 6 Conventional crack classification (Farhidzadeh et al. 2014)

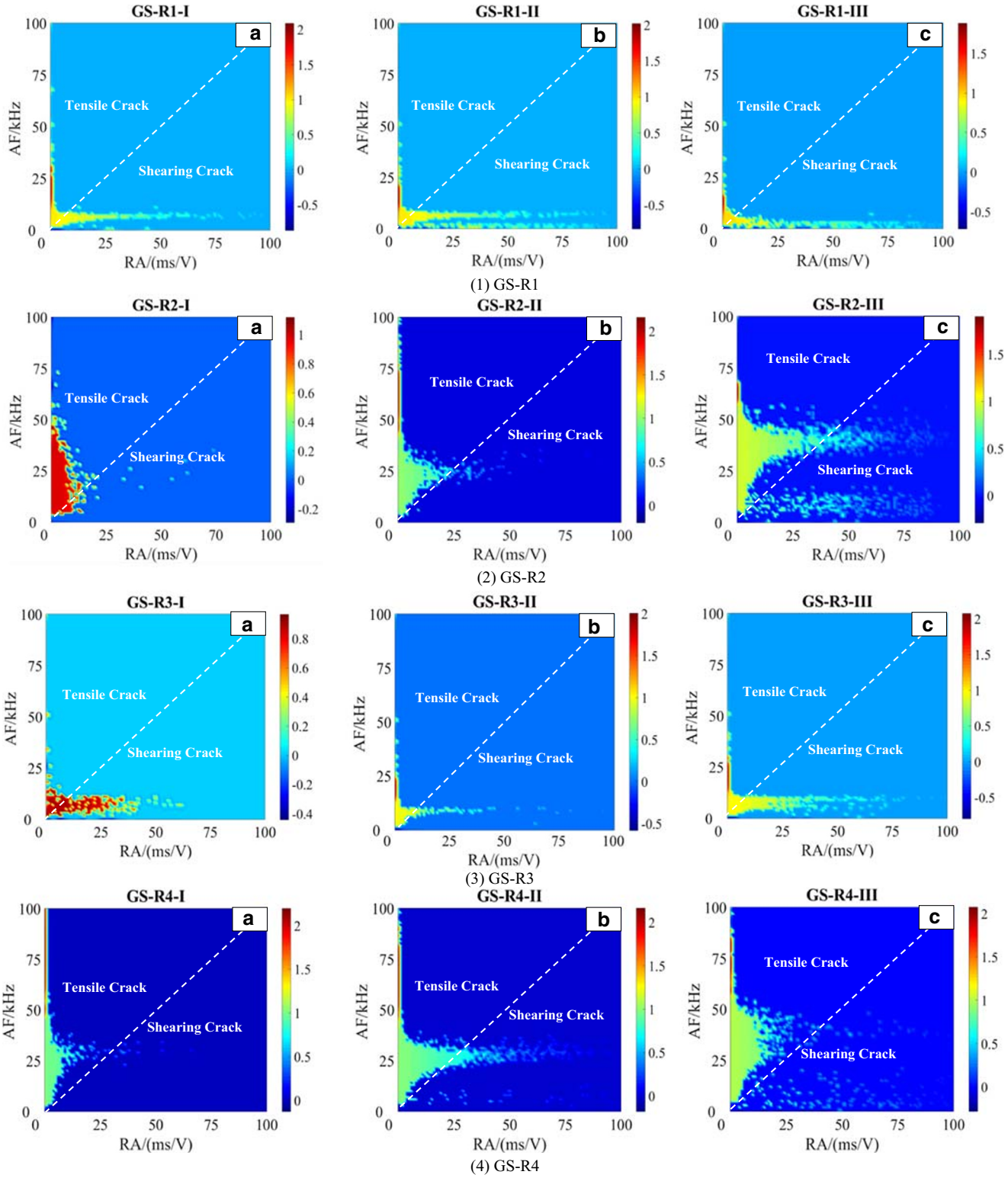

Fig. 7 Density cloud map of RA via AF for each normal force during fracturing evolution

macroscale, main crack presents in *en echelon* type. Based on comparison and observation of crack type in macroscale, failure mode bends failure along the surface that occurred by bond-type damage and then takes the place of shear failure, which is similar to $\mathbf{C1_{12}}$ and $\mathbf{C1_{14}}$ in Fig. 4(1)d, $\mathbf{C2_9}$ and $\mathbf{C2_{10}}$ in Fig. 4(2)d, $\mathbf{C3_9}$ in Fig. 4(3)d, and $\mathbf{C4_{12}}$ in Fig. 4(4)d. Hence, in macroscale, the crack modes of tensile and shearing exist (Fig. 7.c).

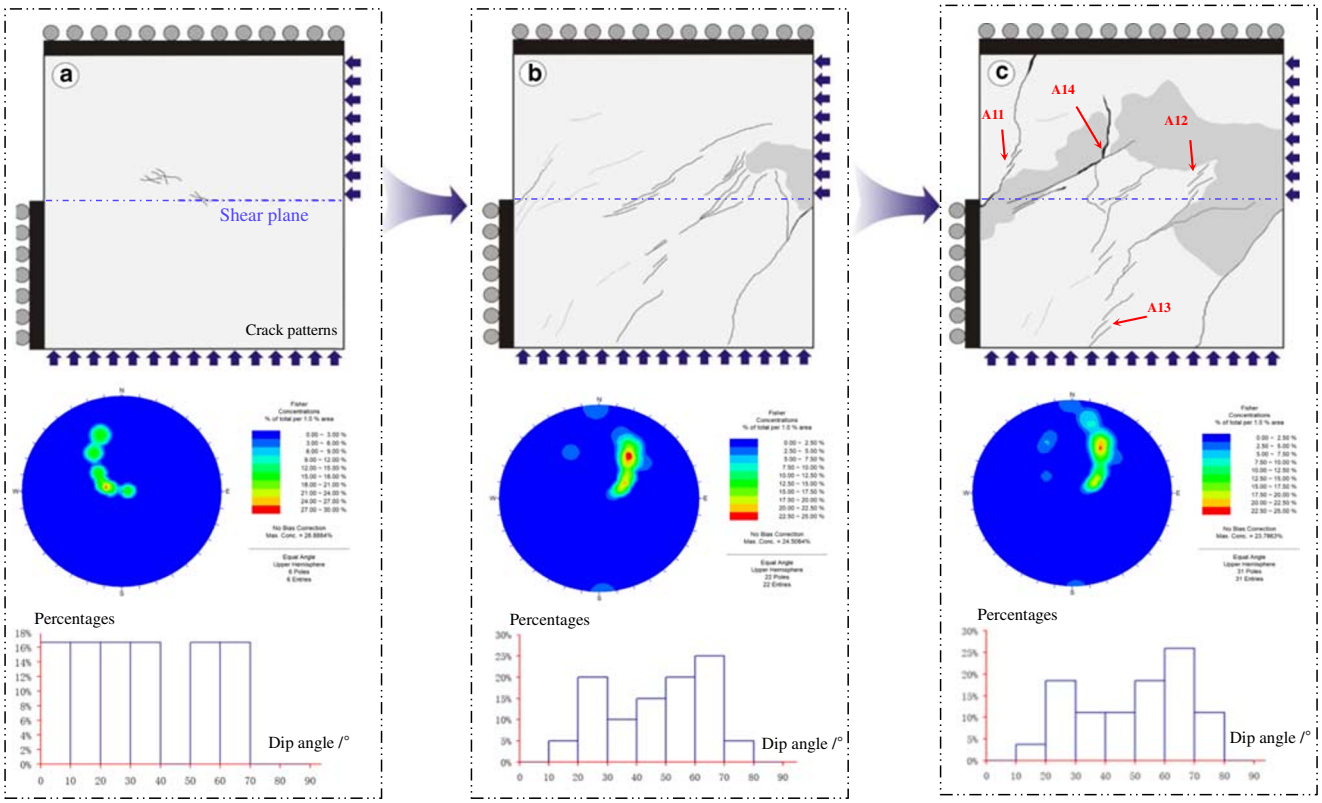

(1) GS-R1

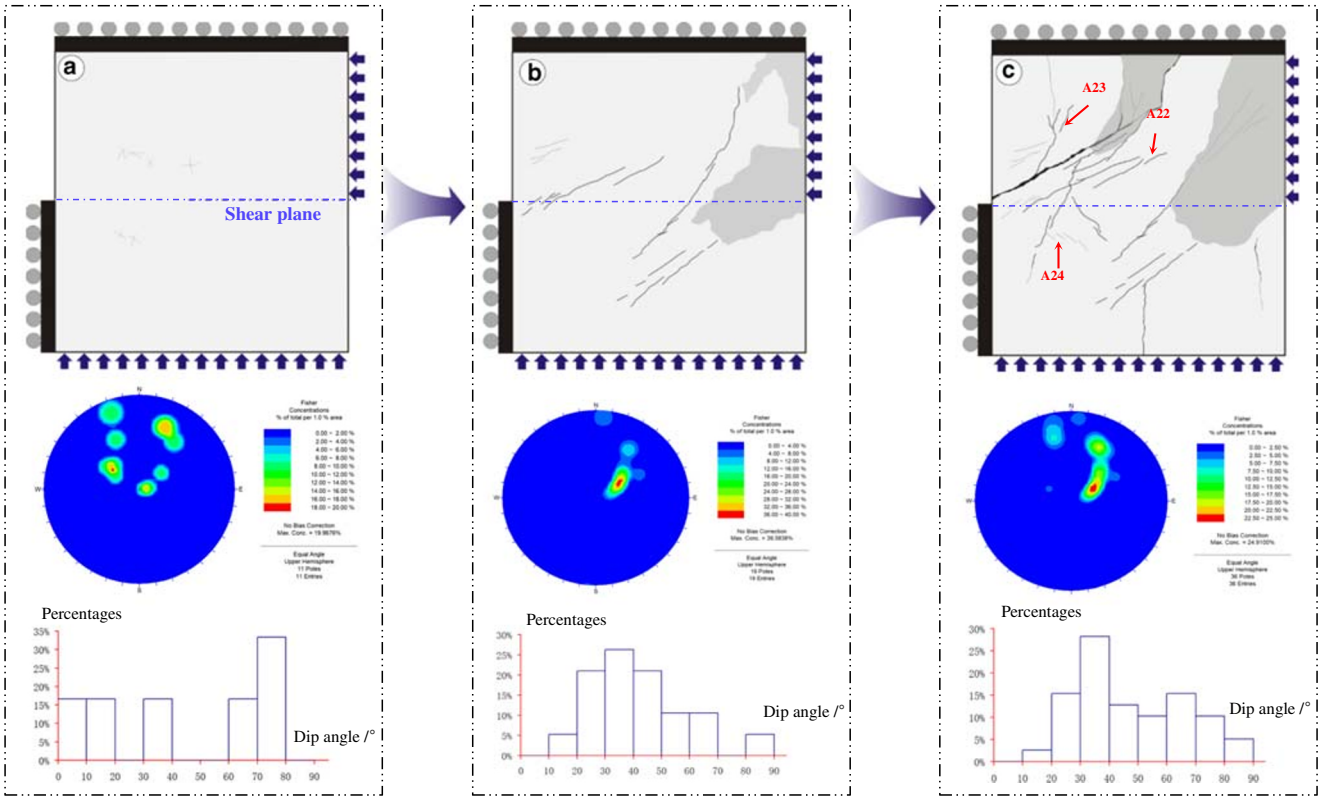

(2) GS-R2

Fig. 8 Development of crack distribution for the different normal stress on different specimens

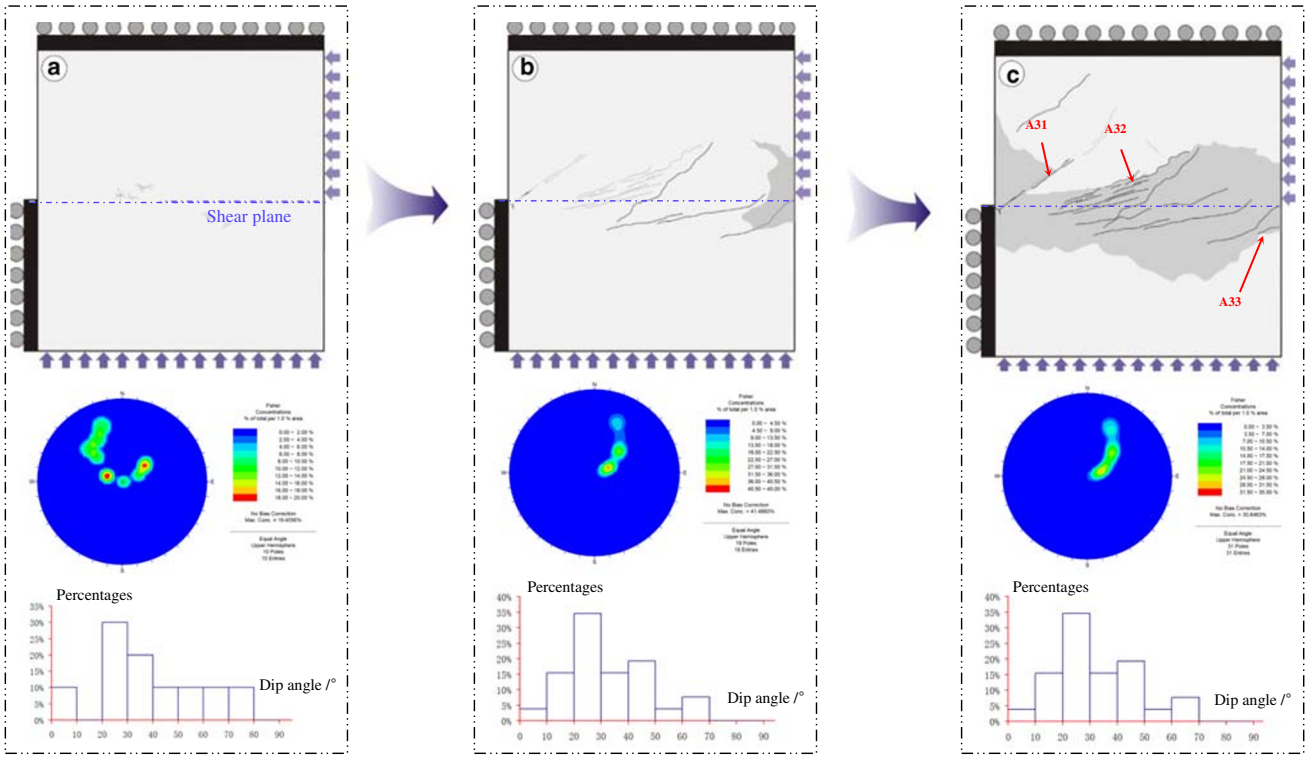

(3) GS-R3

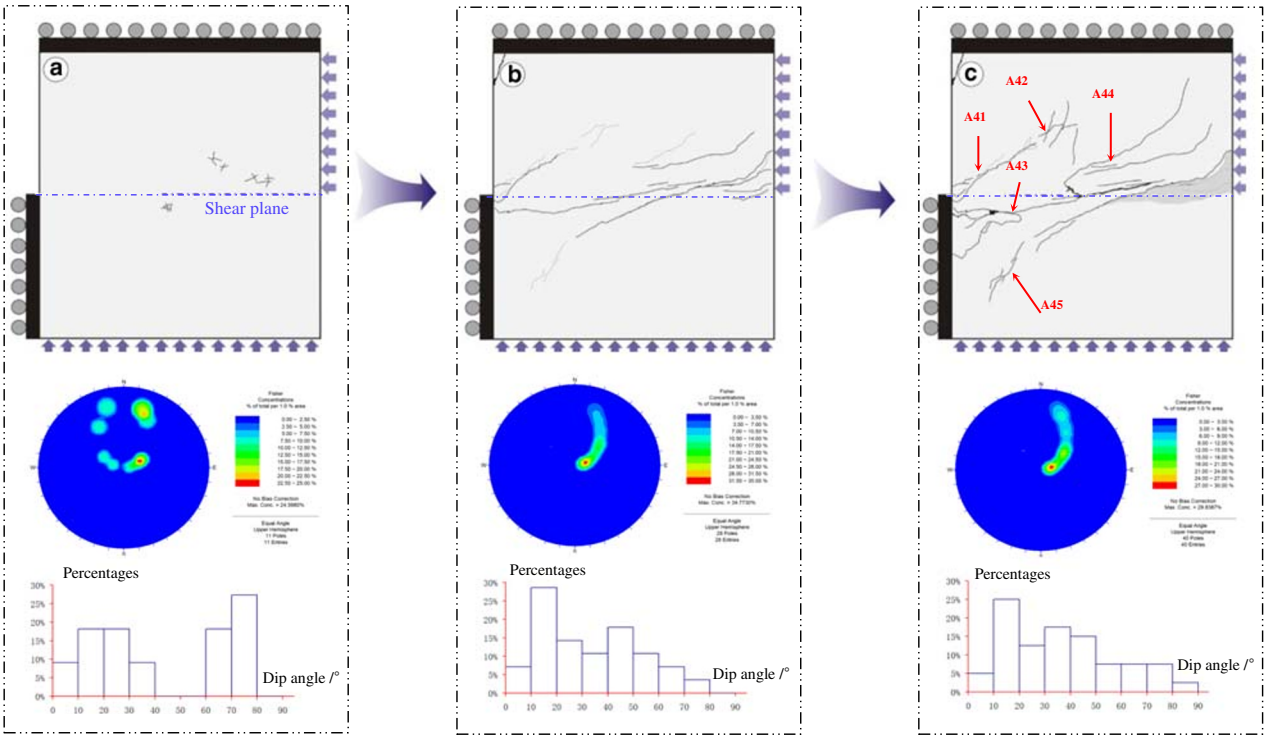

(4) GS-R4

Fig. 8 continued.

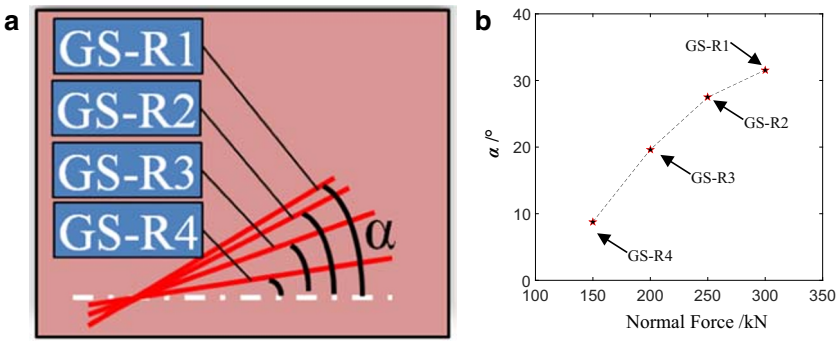

Fig. 9 Statistical relationship diagram of normal force and dip (α) of *echelon*

Discussion

Influencing factors of crack status

The influencing factor of rock physical property was divided into class I and class II, which was self-sustaining fracturing in brittle compression (Akinbinu and Abioye 2016, 2017). Granite belongs to an igneous rock, the minerals that make up rock usually display a wide range of polytropism. Many mineral particles in granite are integrated with crystallization modes, which probably belong to class II.

On the basis of research contents on crack geometry between different normal force, the increase normal force leads to bigger rock constraint and bigger friction force (Fig. 8). There is some relation between crack angle α and normal force σ_1 (Fig. 9). Dip (α) of *en echelon* crack is influenced by normal force σ_1; it exists a positive correlation between σ_1 and α (Fig. 9). The larger the normal force is, the bigger angle of α will be.

Therefore, crack status is influenced by rock physical properties and normal force. Rock physical property is the internal causes of crack status, and normal force is the external causes of crack status.

Characteristics of crack status on crack existence and development aspects

The characteristic of crack status is explored by the aspects of crack existence and development, and described as follows:

1 Crack existence

The most important feature of rock material is the complicated variability of mineral composition in spatial scale. Rock under compression-shearing conditions develops a series of *en echelon* crack in the whole size (macroscale) and many *pinnate* cracks in the local region (localization scale) (crack patterns in Fig. 8). That means the crack existence form "the whole size of *en echelon* crack and the local region of *pinnate* crack."

2 Crack development

Fisher concentrations and crack percentage are used to manifest in the quantification of fracturing evolution (Fig. 8). Continuous activity of fracturing occurs in the same area, which results in the complexity of crack development. Another crack will produce in the same place next time; that is, crack growth inherits in the scale of time. Principal crack forms in early time, and its development follows the law of Inheritance (Fisher concentrations in Fig. 8) and Variability (crack percentage in Fig. 8). Crack development follows the characteristics of "Inheritance and Variability."

Conclusions

(1) Crack status is determined by the internal and external factors, and rock physical property is an internal factor; normal force is an external factor.
(2) Crack existence follows the characteristics of "the whole size of *en echelon* crack and the local region of *pinnate* crack" in terms of spatial-temporal distribution.
(3) Crack development manifests in different spatial-temporal distribution; it manifests a characteristic of "Inheritance and Variability."

However, the influencing factors, such as specimen size, water percentage in rock, rock lithology, and confining stress, are not determined in this research and will be our next research focus.

Acknowledgments All support received by this work is gratefully acknowledged.

Funding This work was supported by the National Natural Science Foundation for Young Scientists of China (No. 51604117, No. 51804122), the National Natural Science Foundation of China (No. 51774138, 41977219), and the State Key Program of National Natural Science of China (No. 41930108).

References

Aharonov E, Scholz CH (2018) A physics-based rock friction constitutive law: steady state friction. J Geophys Res Solid Earth 123(2):1591–1614

Akinbinu, Abioye V (2016) Class I and class II rocks: implication of self-sustaining fracturing in brittle compression. Geotech Geol Eng 34(3):877–887

Akinbinu, Abioye V (2017) Relationship of brittleness and fragmentation in brittle compression. Eng Geol 221:82–90

Alsop GI, Holdsworth RE (2004) Shear zone folds: records of flow perturbation or structural inheritance. Geol Soc Lond Spec Publ 224(1): 177–199

Bost M, Pouya A (2017) Stress generated by the freeze–thaw process in open cracks of rock walls: empirical model for tight limestone. Bull Eng Geol Environ 76(3):1491–1505

Brantut N, Heap MJ, Meredith PG, Baud P (2013) Time-dependent cracking and brittle creep in crustal rocks: a review. J Struct Geol 52(5):17–43

Cheng G, Li L, Zhu W, Yang T, Tang C, Zheng Y, Wang Y (2019) Microseismic investigation of mining-induced brittle fault activation in a Chinese coal mine. Int J Rock Mech Min Sci 123:104096

Clayton JD (2010) Deformation, fracture, and fragmentation in brittle geologic solids. Int J Fract 163(1–2):151–172

Dhahri F, Benassi R, Mhamdi A, Zeyeni K, Boukadi N (2015) Structural and geomorphological controls of the present-day landslide in the Moulares phosphate mines (western-central Tunisia). Bull Eng Geol Environ 75(4):1–10

Engelder T (1989) Analysis of pinnate joints in the Mount Desert Island granite: implications for postintrusion kinematics in the coastal volcanic belt, Maine. Geology 17(6):564–567

Farhidzadeh A, Mpalaskas AC, Matikas TE, Farhidzadeh H, Aggelis DG (2014) Fracture mode identification in cementitious materials using supervised pattern recognition of acoustic emission features. Constr Build Mater 67(2):129–138

Fathi A, Moradian Z, Rivard P, Ballivy G (2016) Shear mechanism of rock joints under pre-peak cyclic loading condition. Int J Rock Mech Min Sci 83:197–210

Hawkes I, Mellor M (1970) Uniaxial testing in rock mechanics laboratories. Eng Geol 4(3):179–285

Ishida T, Labuz JF, Manthei G, Meredith PG, Nasseri MHB, Shin K et al (2017) ISRM suggested method for laboratory acoustic emission monitoring. Rock Mech Rock Eng 50(3):665–674

Janach W, Lan HG (1980) In-plane propagation of shear microcracks in brittle rocks under triaxial compression. J Geophys Res Solid Earth 85(B5):2543–2553

Labaune P, Rouabhi A, Tijani M, Blanco-Martín L, You T (2017) Dilatancy criteria for salt cavern design: a comparison between stress- and strain-based approaches. Rock Mech Rock Eng 51(2): 599–611

Li G, Tang C-a (2015) A statistical meso-damage mechanical method for modeling trans-scale progressive failure process of rock. Int J Rock Mech Min Sci 74:133–150

Li W, Bai J, Cheng J, Peng S, Liu H (2015) Determination of coal-rock interface strength by laboratory direct shear tests under constant normal load. Int J Rock Mech Min Sci 77:60–67

Li XZ, Shao ZS, Fan LF (2016) A micro-macro method for predicting the shear strength of brittle rock under compressive loading. Mech Res Commun 75:13–19

Liu HH, Rutqvist J, Berryman JG (2009) On the relationship between stress and elastic strain for porous and fractured rock. Int J Rock Mech Min Sci 46(2):289–296

Liu G, Cai M, Huang M (2017) Mechanical properties of brittle rock governed by micro-geometric heterogeneity. Comput Geotech 104:358–372

Liu XR, Kou MM, Lu YM, Liu YQ (2018) An experimental investigation on the shear mechanism of fatigue damage in rock joints under pre-peak cyclic loading condition. Int J Fatigue 106:175–184

Meng F, Zhou H, Wang Z, Zhang L, Kong L, Li S et al (2016) Experimental study on the prediction of rockburst hazards induced by dynamic structural plane shearing in deeply buried hard rock tunnels. Int J Rock Mech Min Sci 86:210–223

Misra S, Mandal N, Dhar R, Chakraborty C (2009) Mechanisms of deformation localization at the tips of shear fractures: findings from analogue experiments and field evidence. J Geophys Res Solid Earth 114(B4):1–18

Moore DE, Lockner DA (1995) The role of microcracking in shear-fracture propagation in granite. J Struct Geol 17(1):95–111

Morley CK, Hagke CV, Hansberry R, Collins A, Kanitpanyacharoen W, King R (2018) Review of major shale-dominated detachment and thrust characteristics in the diagenetic zone: part ii, rock mechanics and microscopic scale. Earth Sci Rev 176:19–50

Ohtsu M, Tomoda Y, Suzuki T (2007a) Damage evaluation and corrosion detection in concrete by acoustic emission. In: Carpinteri et al (eds) Fracture mechanics of concrete and concrete structure-design. Assessment and retrofitting of RC structures. Taylor and Francis Group, London

Oyanguren PR, Nicieza CG, Fernández MIÁ, Palacio CG (2008) Stability analysis of Llerin Rockfill Dam: an in situ direct shear test. Eng Geol 100(3):120–130

Pluijm V, Marshak S (2004) Earth structure: an introduction to structural geology and tectonics, 2nd edn. W.W. Norton, New York, pp 124–160

Rathnaweera TD, Ranjith PG, Perera MSA, Silva VRSD (2017) Development of a laboratory-scale numerical model to simulate the mechanical behaviour of deep saline reservoir rocks under varying salinity conditions in uniaxial and triaxial test environments. Measurement 101:126–137

Shiotani T (2008) Parameter analysis. In: Grosse C, Ohtsu M (eds) Acoustic emission testing. Springer, Berlin (Heidelberg), pp 41–51

Sulukcu S, Ulusay R (2001) Evaluation of the block punch index test with particular reference to the size effect, failure mechanism and its effectiveness in predicting rock strength. Int J Rock Mech Min Sci 38(8):1091–1111

Sun QD, Indraratna B, Nimbalkar S (2014) Effect of cyclic loading frequency on the permanent deformation and degradation of railway ballast. Geotechnique 64(9):746–751

Sweta K, Hussaini SKK (2018) Effect of shearing rate on the behavior of geogrid-reinforced railroad ballast under direct shear conditions. Geotext Geomembr 46(3):251–256

Wei Z, Deng X, Sutton MA, Yan J, Cheng CS, Zavattieri P (2011) Modeling of mixed-mode crack growth in ductile thin sheets under combined in-plane and out-of-plane loading. Eng Fract Mech 78(17):3082–3101

Winter MJ, Hyodo M, Wu Y, Yoshimoto N, Hasan MB, Matsui K (2017) Influences of particle characteristic and compaction degree on the shear response of clinker ash. Eng Geol 230:32–45

Xu J, Zhai C, Qin L, Yu G (2017) Evaluation research of the fracturing capacity of non-explosive expansion material applied to coal-seam roof rock. Int J Rock Mech Min Sci 94:103–111

Zhou XP (2005) Localization of deformation and stress–strain relation for mesoscopic heterogeneous brittle rock materials under unloading. Theor Appl Fract Mech 44(1):27–43

Zhou SW, Xia CC, Hu YS, Zhou Y, Zhang PY (2015) Damage modeling of basaltic rock subjected to cyclic temperature and uniaxial stress. Int J Rock Mech Min Sci 77:163–173